iScience

CellPress
OPEN ACCESS

Article

Critical role of NiO support morphology for high activity of Au/NiO nanocatalysts in CO oxidation

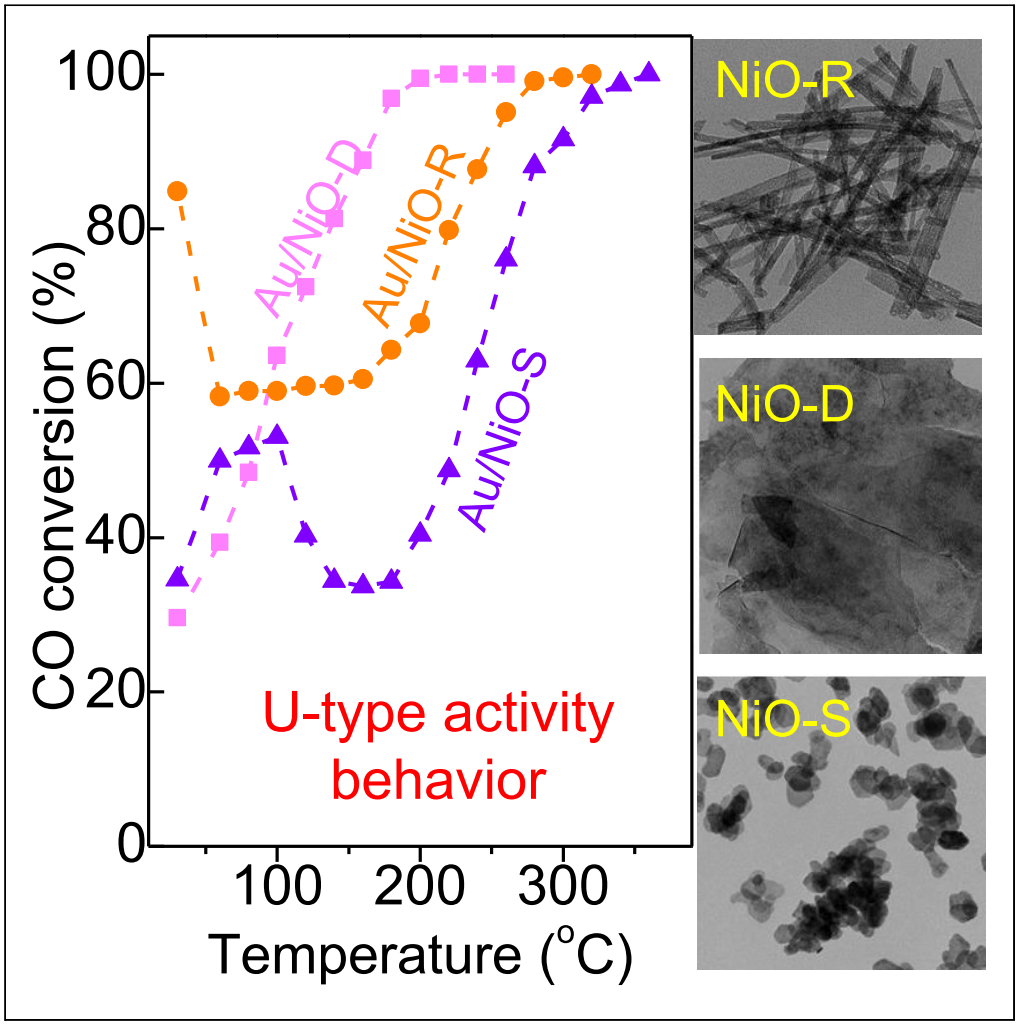

Sami Barkaoui, Yanrong Wang, Yifei Zhang, ..., Binli Wang, Gao Li, Zhen Zhao

bl.wang@siat.ac.cn (B.W.)
gaoli@dicp.ac.cn (G.L.)
zhenzhao@cup.edu.cn (Z.Z.)

Highlights

The morphology effect on catalytic behavior is investigated in gold-catalyzed CO oxidation

Au/NiO-R and Au/NiO-D show an atypical behavior of U-shaped curve of activity vs. temperature

Au/NiO-R shows a rate of 1.78 $mol_{CO}\ g_{Au}^{-1}\ h^{-1}$, among the higher rates reported so far for Au-based systems

DRIFTS measurement identifies $Au^{\delta+}$ species as crucial CO adsorption site promoting CO oxidation at low T

Barkaoui et al., iScience 27, 110255
July 19, 2024
https://doi.org/10.1016/j.isci.2024.110255

iScience

CellPress
OPEN ACCESS

Article

Critical role of NiO support morphology for high activity of Au/NiO nanocatalysts in CO oxidation

Sami Barkaoui,[1,2,5] Yanrong Wang,[1,5] Yifei Zhang,[1,2] Xinrui Gu,[2,4] Zhiwen Li,[2] Binli Wang,[3,*] Gao Li,[1,2,4,6,*] and Zhen Zhao[1,5,*]

SUMMARY

The effect on catalytic behavior induced by different morphology of NiO supports has been investigated using the example of gold-catalyzed CO oxidation. Three NiO-supported nanogold consisting of nanogold deposited onto NiO nanorods (NiO-R), nanosheet (NiO-S), and nanodiscs (NiO-D) were prepared. Transmission electron microscopy(TEM)/Scanning transmission electron microscopy(STEM) investigations indicated that Au particles dominantly exposed Au(111) facets virtually independent of NiO architectures. Au/NiO-S displayed a normal Arrhenius-type behavior. Au/NiO-R and Au/NiO-D showed an atypical behavior, characterized by a U-shaped curve of activity vs. temperature, which is attributed to the carbonate accumulation on whose catalytically active sites. On Au/NiO-R, a stable CO-conversion rate of 1.78 $mol_{CO}\ g_{Au}^{-1}\ h^{-1}$ at 30°C was achieved, which is among the higher rates reported so far for supported Au-based systems. DRIFTS measurement identified $Au^{\delta+}$ species as crucial CO adsorption sites promoting CO oxidation, and the catalytic CO oxidation should obey Mars-van Krevelen (<200°C) and Eley-Rideal mechanism (>240°C).

INTRODUCTION

Carbon monoxide oxidation is a crucial catalytic reaction for air pollution control and is relevant in various chemical processes, including the removal of CO in car exhaust streams[1] and the elimination of poisonous CO from synthesis gas streams for upgrading hydrogen gas used as fuel for low-temperature fuel cells.[2,3] Heterogeneous catalysis by gold has advanced immensely since the pioneering work of Haruta et al.[4] reporting astoundingly high activity in low-temperature CO oxidation of very small (<5 nm) Au nanoparticles (NPs) deposited on base metal oxides. The size-dependent catalytic activity of supported nanogold catalysts is an exciting topic in Au catalysis[5,6] and has been studied widely.[7,8] By decreasing the size of Au particles, their electronic structure, including the quantum size effect, and Au-support perimeter interface can be modulated leading to improved catalytic activity and selectivity.[8] Due to their unique properties, Au NPs have a large application range,[9] which differs from that of Au in bulk form. Bulk gold is mostly poorly active as a catalyst, but in the form of Au NPs, it can exhibit exceptional catalytic activity.[10,11] Reactions catalyzed by supported Au NPs comprise e.g., various redox reactions,[11,12] catalytic CO oxidation,[12–14] oxidation of alcohols,[15] hydrogenation of nitrophenol,[16–18] and selective epoxidation.[19,20] Au NPs are also excellent catalysts for reactions involving alkyne activation due to their Lewis acid nature.[21,22] Though the catalytic activity of Au NPs depends on numerous factors, it is largely determined by the particle size.

Another crucial factor determining the catalytic performance of gold catalysts is the nature of the oxide support.[23–26] Reducible metal oxide supports, such as CeO_2, NiO, Co_3O_4, ZrO_2, generally lead to more efficient nanogold catalysts than non-reducible oxides (e.g., MgO, SiO_2) in CO oxidation.[27,28] NiO is an earth-abundant transition metal oxide with superior properties in redox processes, gas sensing, and electrochemical devices. Researchers have investigated NiO catalysts with numerous shapes for CO oxidation and established that flower-like and ring-like NiO[29] exhibit high activity. To our knowledge there exist only a few reports about the Au/NiO-catalyzed CO oxidation.[29–32] With one exception[33] they all were based on supported Au particles. Recently, Au single-atom catalysts supported on defective NiO as stabilizer were developed by Murayama's group. These catalysts show outstanding activity and stability and seem to offer high potential for CO oxidation.

Herein we explored the effect of morphology of NiO supports decorated with Au NPs and examined the behavior of these catalysts in CO oxidation. With certain NiO architectures, an anomalous activity behavior has been observed, characterized by a U-shaped activity curve. The

[1]Institute of Catalysis for Energy and Environment, College of Chemistry and Chemical Engineering, Shenyang Normal University, Shenyang 110034, China
[2]State Key Laboratory of Catalysis, Dalian Institute of Chemical Physics, Chinese Academy of Sciences, Dalian 116023, China
[3]Shenzhen Institute of Advanced Technology, Chinese Academy of Sciences, Shenzhen 518055, China
[4]University of Chinese Academy of Sciences, Beijing 100049, China
[5]These authors contributed equally
[6]Lead contact
*Correspondence: bl.wang@siat.ac.cn (B.W.), gaoli@dicp.ac.cn (G.L.), zhenzhao@cup.edu.cn (Z.Z.)
https://doi.org/10.1016/j.isci.2024.110255

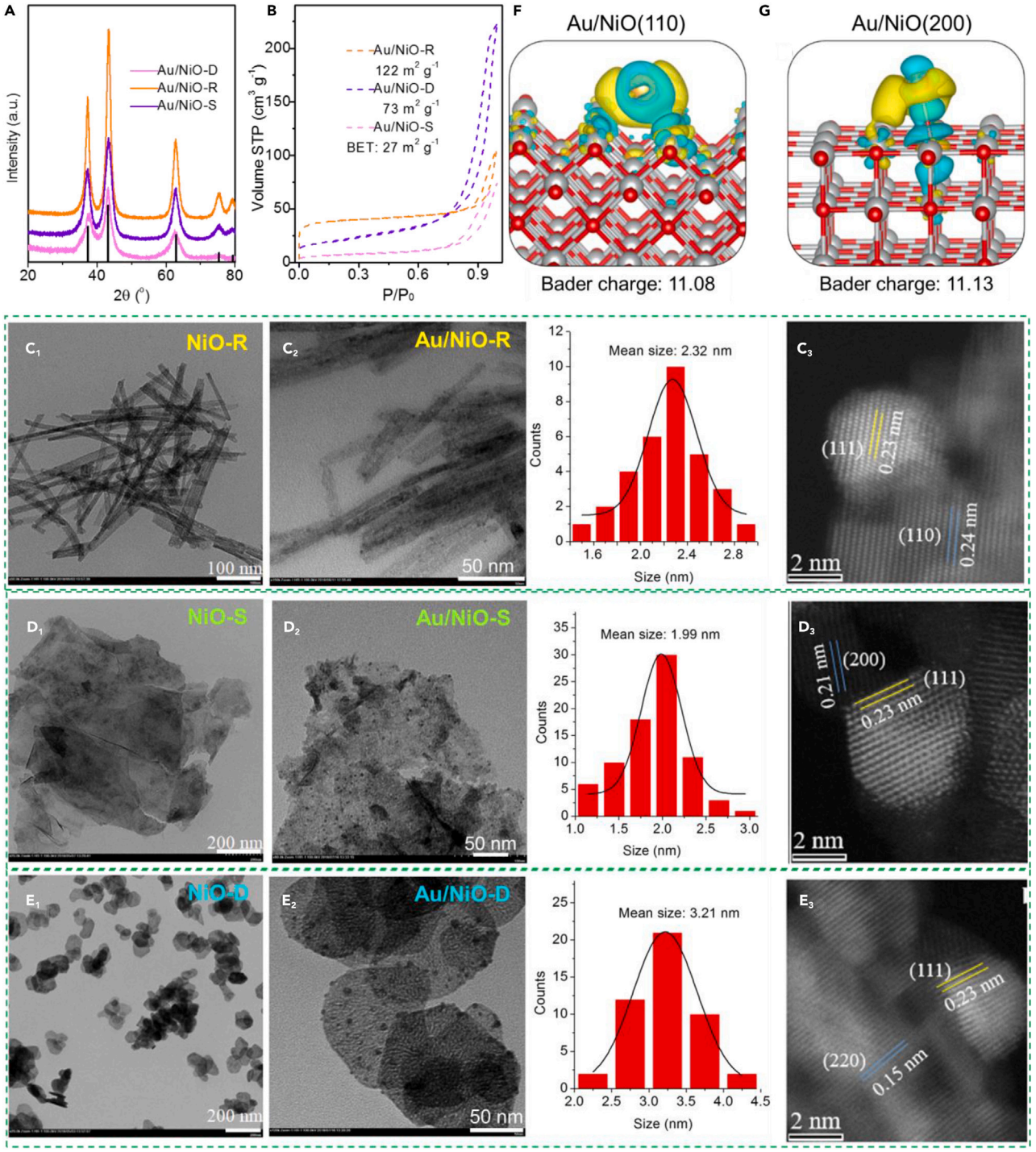

Figure 1. The characterization of the NiO-supported gold nanoparticles

(A and B) (A) XRD patterns of the morphologically different Au/NiO catalysts and (B) N_2 adsorption-desorption isotherms. The hysteresis at high p/ps is attributed to the void space between the nanoparticles and not to pores in the nanostructured materials.

(C–E) TEM images of the NiO supports: (C1) NiO-R, (D1) NiO-S, and (E1) NiO-D. TEM images with the related histograms of the deposited Au NPs of the Au/NiO samples: (C2) Au/NiO-R, (D2) Au/NiO-S, and (E2) Au/NiO-D. STEM images indicate that the deposited Au particles mainly exposed the (111) facets. Depending

Figure 1. *Continued*

on the shape of the support particles the facets exposed dominantly were (C3) NiO-R(110), (D3) NiO-S(200), and (D4) NiO-D(220). See also TEM images S1-S2 in Supporting Information.

(F and G) Charge density difference analysis for Au/NiO hetero-structures: (F) Au on NiO(110) and (G) Au on NiO(200). The isosurface of the electron density difference was plotted at a value of about 0.002 electron Å−1, and the blue and yellow isosurfaces represent the electron depletion and accumulation regions, respectively. The bader charge of the adsorptive Au is shown below the figure.

study revealed that the morphology and shape of NiO support NPs have a decisive influence on catalytic performance and stability of these gold catalysts. These experimental results are further corroborated by computational simulations.

RESULTS

Characterization of NiO-supports and corresponding Au/NiO catalysts

The different morphologies and shapes of the synthesized NiO-supported Au catalysts, nanorods (NiO-R), nanosheets (NiO-S), and nanodiscs (NiO-D) were examined employing XRD, transmission electron microscopy (TEM), and scanning transmission electron microscopy (STEM). XRD patterns of the Au/NiO catalysts within the 2θ range of 20°–80° are presented in Figure 1A. The diffraction lines at 37.2°, 43.2°, 62.7°, and 75.4°, are associated with the cubic NiO faces (111), (200), (220), and (311) (JCPDS no. 47–1049), respectively. No reflections belonging to Au particles were detected in the XRD patterns, which is attributed to the relatively low Au loading (~0.90 wt %) and high dispersion of the very small Au particles (~2–3 nm, Figure 1A). The nanocatalysts exhibited type-IV nitrogen adsorption-desorption isotherms at high P/P_0 (Figure 1B), which should be attributed to the void volume between the particles because TEM investigations showed no indication of mesopores in the NPs. The BET surface areas and pore distributions by Barret-Joyner-Halenda method were Au/NiO-R (122 $m^2\ g^{-1}$, 28.5 nm), Au/NiO-D (73 $m^2\ g^{-1}$, 37.8 nm), and Au/NiO-S (27 $m^2\ g^{-1}$, 15.8 nm), Figure S3.

Typical TEM images of the different shapes of the pure NiO supports are presented in Figure 1. The support particles had the following dimension ranges: NiO-R (diameters 10 to 15 nm), NiO-D (length ~110 nm, thickness ~15 nm), and NiO-S (thickness ~5 to 6 nm). The Au NPs were deposited on the surface of the different NiO samples using an Au-PVA colloid of 2.32 nm for Au/NiO-R, 1.99 nm for Au/NiO-S, and 3.2 nm for Au/NiO-D. Comparison of TEM images before and after Au deposition (Figures 1C–1E) confirmed that the NiO morphology in the corresponding Au/NiO samples was virtually preserved after removal of the PVA by calcination at 300°C, which is ascribed to the strong support-metal interaction (SMI) between the gold particles and the NiO supports. Figure 1C shows a typical STEM image of NiO-R, indicating that the predominantly exposed facet is the (110) crystal plane with an inter-planar spacing of 0.24 nm.[34] Figure 2F indicates that for Au/NiO-S, the measured inter-planar distance of 0.21 nm, which matches the (220) crystal plane of the cubic crystalline NiO, suggesting that the growth plane of the nanosheets is along the (200) planes.[35] For Au/NiO-D, the measured inter-planar distance of 0.15 nm corresponds to the (220) crystal plane of cubic NiO, as shown in Figure 1I).[36] Figures 1C, 1F, and 1I confirm that the deposited Au NPs exposed dominantly (111) facet with a d-spacing of 0.23 nm on the different NiO architectures. As visualized in Figures 1F and 1G, we simulated the formation of Au/NiO(110) and Au/NiO(200), respectively. As a result, the interaction between Au and NiO(110) is stronger with the analysis of electron density difference; while the bader charge is lower, accordant with the active $Au^{\delta+}$ species.

Chemical state of Au/NiO surface

X-ray photoelectron spectroscopy (XPS) analyses were performed to investigate the chemical state of the Au/NiO catalysts. The spectra of Ni 2p, O 1s and Au 4f of Au/NiO-D, Au/NiO-R, and Au/NiO-S are shown in Figure 2. The Ni 2p signal could be deconvoluted into five peaks, where the three binding energies (B.E.) at 854.1, 856.4, and 861.2 eV are attributed to Ni 2p3/2, and the peaks at 873.7 and 880.2 eV to Ni 2p1/2. The two peaks located at 854.1 and 861.2 eV are typical for Ni^{2+} in NiO.[37] As mentioned previously, NiO, as a p-type semiconductor, favors the formation of Ni^{2+} defects, which usually induce the generation of Ni^{3+} for charge neutrality.[37] The signal of Ni^{3+} should be in the range 856.1–856.4 eV, indicating that the peak at 856.4 eV could be assigned to Ni^{3+}. The position of the peaks for Au/NiO-D, Au/NiO-R, and Au/NiO-S is almost the same, close by the value of pure NiO (854.2 eV), with a little shift of the binding energy.[38]

The O1s electronic levels for as-prepared catalysts were also studied; the asymmetric O1s could be deconvoluted into two peaks at 531.6 and 529.6 eV for Au/NiO-R, Au/NiO-D, and Au/NiO-S. The XPS peak at 529.6 eV was attributed to surface lattice oxygen (O_{latt}) species and the 531.6 eV peak to adsorbed oxygen (O_{ads}) species on NiO.[39] On the other hand, for Au/NiO-S (Figure 2I), the peak at around 529.5 eV is characteristic of surface lattice oxygen. The peak at around 531.4 eV could be assigned to loosely bonded oxygen.[39] The calculated surface O_{ads}/O_{latt} atomic ratios of all samples are presented in Figure 3D. Note that the O_{ads}/O_{latt} ratio followed the order Au/NiO-R > Au/NiO-D > Au/NiO-S. These results are in line with the higher activity of CO oxidation measured over Au/NiO-R and Au/NiO-D compared to Au/NiO-S at 30°C. As depicted in Figures 2A, 2D and 2G, the XPS spectra of three catalysts Au/NiO-R, Au/NiO-D, and Au/NiO-S show the binding energy of Au 4f7/2 at 84.2 eV, which is a little higher than that for neutral metallic Au (83.9 eV)[40] suggesting the formation of $Au^{\delta+}$ species due to electron transfer from the Au NPs to the NiO support.

Catalytic behavior

For most CO oxidation catalysts based on supported gold or metal oxides, a "normal" activity behavior (an increase of reaction rate with temperature) is observed. An atypical activity behavior was observed with some of the present Au/NiO catalysts. Figure 3A shows a U-type activity vs. temperature curve for Au/NiO-R and Au/NiO-S, characterized by varying of the apparent activation energy (Ea) with temperature. In

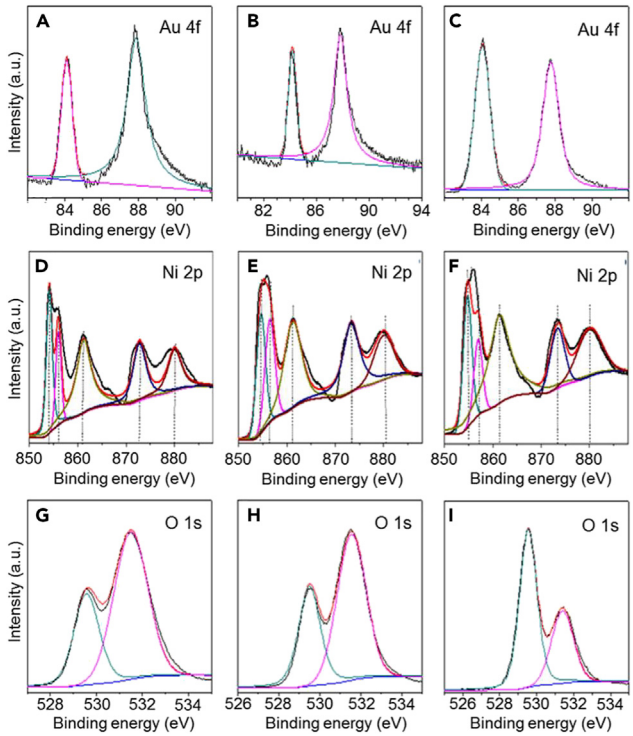

Figure 2. XPS analyses

The Au 4f, Ni 2p and O 1s XPS survey spectra of (A, D, and G) Au/NiO-D, (B, E, and H) Au/NiO-R, and (C, F, and I) Au/NiO-S.

contrast, Au/NiO-D exhibited a normal Arrhenius-type temperature dependence of activity with an Ea ~13.7 kJ mol^{-1} (Figure S4) in the temperature range from 30°C to 150°C. The U-type activity behavior results from the superposition of two simultaneously occurring processes, CO oxidation and catalyst deactivation, which differently depend on temperature. The pure NiO supports were almost inert at temperatures below 150°C under the conditions used (Figure 3A). The highest CO conversion was observed for NiO-R support, while the conversions of NiO-D and NiO-S were considerably lower (less than 2% CO conversion). Temperature-programmed desorption profiles on BET surface areas of preadsorbed CO_2 are shown in Figure 3B. Desorption of CO_2 on Au/NiO-D did barely occur at T < 150°C and was much lower also at higher temperatures compared to that observed with Au/NiO-R and Au/NiO-S, although the BET surface area of Au/NiO-D in-between the three Au/NiO samples (Figure 3B). It manifests that the evolving CO_2 species is prone to dissociate from Au/NiO-D (main exposing NiO(220) facet) surface rather than Au/NiO-R (chief NiO(110) facet), and Au/NiO-S (NiO(200) (f). Therefore, the catalysts exhibiting U-type conversion curves (Au/NiO-R and Au/NiO-S) show rather complex CO_2 desorption profiles that the formed carbonate or bicarbonate ions on the catalytically active sites of Au/NiO-R and Au/NiO-S, resulting in the retardation of catalytic CO oxidations. The catalytic CO oxidation over Au/NiO composites should obey Eley-Rideal mechanism, that is, both CO and O_2 are adsorbed and activated over the gold particles at high reaction temperatures (e.g., > 240°C).[13] Figure 3C shows the long-term stability tests of the catalysts at 30°C. All catalysts showed an initial induction period where the CO consumption rate decreased and finally reached a nearly steady state. It is worth noting that no evident sintering of Au NPs was observed in TEM analysis of these spent Au/NiO catalysts (Figure S5).

With the best-performing catalyst, Au-NiO-R, a stable rate of 1.78 mol_{CO} g_{Au}^{-1} h^{-1}, was achieved, which is one of the highest rates reported so far with Au/NiO-based systems,[29–31] U-type conversion curves have also been observed previously for Au/NiO catalysts with different structural architectures. Xu et al.[30] demonstrated that Au NPs decorated with highly dispersed NiO nanopatches, so-called inverse Au-NiO catalysts, are highly active for CO oxidation and can exhibit a U-type activity behavior. Zhou et al.[31] reported the synthesis of Ni-Au alloy NPs and their use in preparing silica-supported Au/NiO nanomaterials for catalytic CO oxidation.

The U-shape behavior for the temperature dependence of activity was also reported for other catalysts Au/$Mg(OH)_2$,[41] Au/MgO,[42,43] and Co_3O_4-SiO_2.[44] In the case of Au/$Mg(OH)_2$, this behavior was attributed to the strong interactions with carbonate species or adsorbed CO_2, which block the reaction sites and inhibit CO_2 desorption. A decrease in the initial activity (induction period) was also observed with Au/$Mg(OH)_2$. On Co_3O_4-SiO_2, trace amounts of water (less than 3 ppm) induced a decrease in the catalytic activity. Such complex U-shaped curves of activity indicate the existence of competing processes occurring on the catalyst surface. In the present case, the U-shape activity behavior over the different Au/NiO composites is most likely associated with the interaction of CO_2 with hydroxyl radicals (e.g., carbonates).

Furthermore, it has been established that the CO oxidation reaction over Au NPs can occur through low-temperature and high-temperature reaction mechanisms.[45] In the low-temperature range, CO molecules mostly react with weakly adsorbed O_2 or surface (-OH) groups. Increasing the reaction temperature lowers the coverage of weakly adsorbed oxygen-containing surface species, which lessens the catalytic activity. The

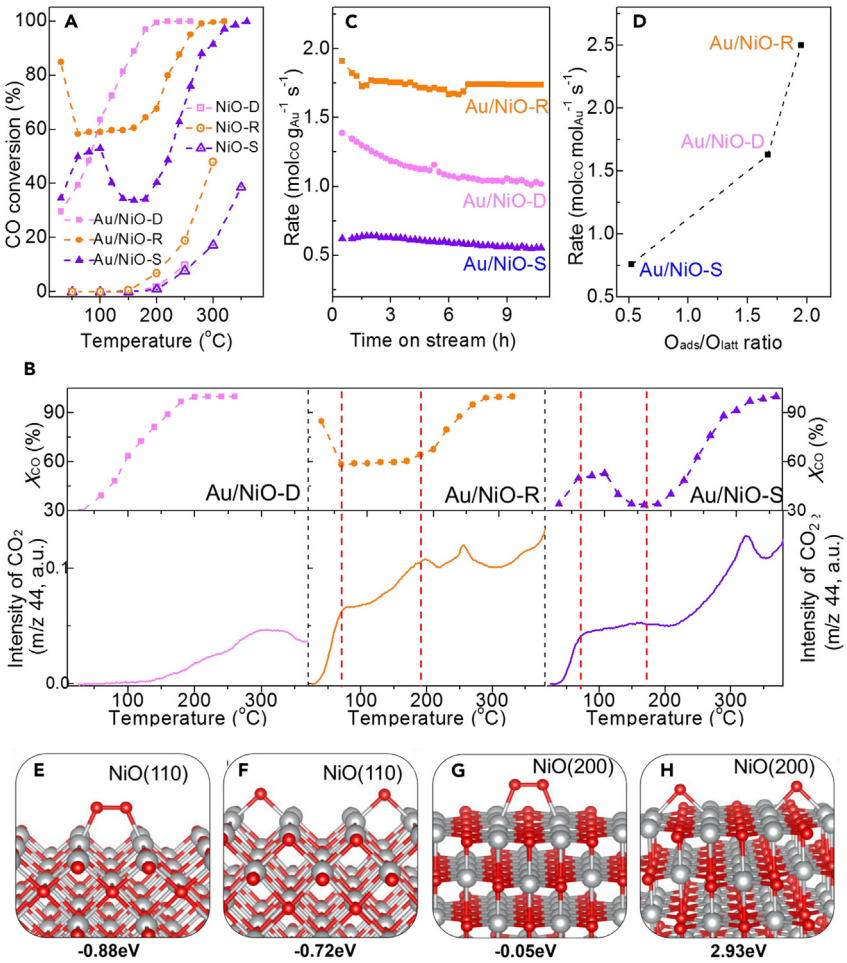

Figure 3. The catalytic performance in the CO oxidations

(A) Catalytic behavior of the Au/NiO catalysts and pure NiO supports in the CO oxidation investigated by temperature-programmed reaction. Reaction conditions: Reactant gas mixture,1%CO/20%O_2 balanced with He, flow rate 50 mL min^{-1}, 50 mg catalyst, GHSV 60,000 mL g_{cat}^{-1} h^{-1}.

(B) The relationship of CO_2 desorption profiles and catalytic activity.

(C) Long-term stability tests of Au/NiO catalysts. Test conditions: reactant gas mixture, 1%CO/20%O_2 balanced with He, flow rate 50 mL min^{-1}, GHSV 60,000 mLg_{cat}^{-1} h^{-1}, reaction temperature of 30°C.

(D) Initial CO consumption rates at 30°C versus O_{ads}/O_{latt} ratio. Conditions as in Figure 4B. Conditions of measurements of the CO_2 desorption profiles are described in the Experimental Part.

The optimized structure molecular O_2 and dissociative O_2 on (E and F) NiO(110) and (G and H) NiO(200). The adsorption energy upon the bare surface and isolated molecule are shown.

theoretical simulation results of adsorption and conversions for O_2 on NiO(110) and NiO(200) surfaces are shown in Figures 3F–3H. The calculated adsorption energy for molecular O_2 on NiO(110) is −0.88 eV, indicating the relative stronger adsorption on 4-coordinated surface Ni (Ni_{4c}), Figure 3E. And the dissociation for the O-O bond in the adsorptive O_2 is feasible with a reaction energy of 0.16 eV (Figure 3F), which facilitates the further CO oxidation. In comparison, the adsorption of O_2 molecules on NiO(200) with 5-coordinated surface Ni (Ni_{5c}) is rather difficult (−0.05 eV, Figure 3G), while the O_2 dissociation is prohibit with relative high reaction energy (2.98 eV, Figure 3H). Thus, the NiO(110) exhibits better capacity to activate the O_2 molecules than NiO(200), consistent with the observed experimental results. And the O_2 activation over these Au/NiO catalysts should obey the Epling-Xu mechanism during the aerobic CO oxidation.[46] And the formed carbonate or bicarbonate species on the NiO oxide supports occupy the active sites for O_2 decomposition, which results in the U-shaped relations of CO oxidation activity vs. temperature in the systems of Au/NiO-R and Au/NiO-S catalysts. In contrast, in the high temperature region, in which CO oxidation activity shows a normal Arrhenius-type behavior, O_2 can dissociate on the Au surface. The U-shaped activity curve could therefore also originate from the transition of low-temperature to high-temperature mechanism,[43] which in turn is affected by the capability of the catalyst to provide reactive oxygen at different temperatures.[44] The rate of 1.78 mol_{CO} g_{Au}^{-1} h^{-1} achieved with the Au/NiO-R catalyst (Figure 3C) is within the highest reaction rates reported in the literature for other Au/NiO composites (e.g., 1.74 mol_{CO} g_{Au}^{-1} s^{-1} of Au-Ni/SiO_2[30] and 1.63 mol_{CO} g_{Au}^{-1} s^{-1} of Ni-Au/SiO_2[31]) and generally for Au-based systems.[47–49] However, an outstanding exception represents the Au

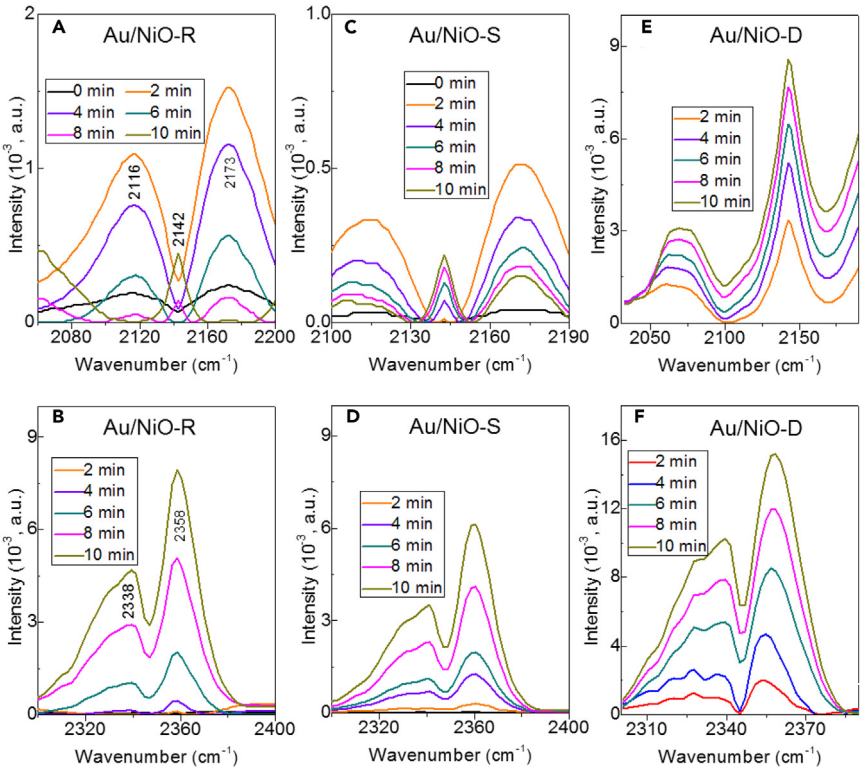

Figure 4. DRIFTS analyses

DRIFTS spectra of CO adsorption on as-prepared Au/NiO catalysts with different morphologies: (A and B) Au/NiO-R, (C and D) Au/NiO-S, and (E and F) Au/NiO-D.

single-atom catalysts supported on NiO reported recently by Mochizuki et al.[33] These Au single-atom catalysts exhibit an outstanding activity for CO oxidation, which exceeds that of all other nanoparticulate Au/NiO catalysts. Figure 3D demonstrates that the activity of the present Au/NiO catalysts is strongly related to the proportion of adsorbed oxygen to lattice oxygen (O_{ads}/O_{latt}) determined by XPS, which indicates that this ratio is crucial for the governing reaction mechanism (e.g., Mars-van Krevelen (MvK) mechanism at low reaction temperature (<200°C).[28]

Diffuse reflectance infrared fourier transform spectroscopy (DRIFTS)

DRIFTS of adsorbed CO was used to examine the state of the surface gold atoms and the CO adsorption on the catalysts at room temperature.[50] Figure 4 shows that the intensity and the shape of the band due to CO adsorbed on the Au/NiO catalysts are very different. The CO adsorption on Au/NiO-R and Au/NiO-S at room temperature gave rise to three bands in the carbonyl stretching region, their maxima being located at 2116, 2142, and 2172 cm^{-1}, respectively. The band observed at 2116 cm^{-1} can be assigned to Au^0-CO and the 2142 cm^{-1} frequency region can be attributed to CO molecules adsorbed on partially positive charged gold $Au^{\delta+}$-CO ($0 < \delta < 1$),[51] while the band at 2172 cm^{-1} is attributed to CO adsorption on Au^+ (CO-Au^+).[52] Interestingly, with Au/NiO-R and Au/NiO-S, the signal of Au^0-CO (2116 cm^{-1}) and Au^+-CO (2172 cm^{-1}) rapidly decreased while the peak of $Au^{\delta+}$-CO (2142 cm^{-1}) increased during the CO adsorption process. For Au/NiO-D, the band at 2142 cm^{-1} can be attributed to CO molecules adsorbed on partially positive charged gold $Au^{\delta+}$-CO ($0 < \delta < 1$). Simultaneously, another absorption band appeared at 2064 cm^{-1}, which is attributed to CO adsorbed on a negatively charged gold surface.[53]

As shown in Figure 4, the intensity of the two bands at 2143 cm^{-1} and 2064 cm^{-1} gradually increased during the CO adsorption process. The $Au^{\delta+}$ species have a stronger CO adsorption ability resulting in higher catalytic activity. $Au^{\delta+}$ sites appear to play a significant role at least as adsorption sites for CO oxidation. The activity enhancement of Au/NiO-R and Au/NiO-S can be attributed to the partial transition from Au^+ to $Au^{\delta+}$. To gain deeper insight into the origin of the high activity and the deactivation of Au catalysts, the formation of surface species on the Au/NiO catalysts during reactions at RT has been tracked by DRIFTS measurements under identical reaction conditions. As shown in Figures 4D, a strong band due to gaseous CO_2 appeared, as indicated by the presence of the P and R branches at 2338 cm^{-1} and 2360 cm^{-1}. For Au/NiO-R and Au/NiO-S catalysts, the interaction between CO_2 and the support is weak enough to allow for CO_2 desorption and therefore the continuous formation of gaseous CO_2. This is in good agreement with the observation of substantial amounts of CO_2 gas in the desorption measurements (Figure 3D). It can be proposed that the partial loss of activity in the initial period of the stability tests at 30°C (Figure 3B) is caused by the competing processes of CO oxidation and catalyst deactivation due to the formation of surface carbonate species, which either block active sites or hinder access of reactants to these sites.[54,55]

Such kind of site blocking by the activated formation of carbonate species could also explain the absence of high catalytic CO oxidation activity if the temperature is below 160°C on Au/NiO-R, and Au/NiO-S, and below 60°C on Au/NiO-D. The slower formation of surface carbonate species at temperatures higher than 160°C for Au/NiO-R and Au/NiO-S, and higher than 60°C for Au/NiO-D may be due to either an activation barrier for this process or to surface blocking ("competitive adsorption") by CO_{2ad}. As shown in Figure 4D, the bands in the spectra at 2338 cm^{-1} and 2260 cm^{-1} stand for the formation of CO_2. The drifts of CO_2 signals increase in the order Au/NiO-D > Au/NiO-R > Au/NiO-S, in line with the higher catalytic activity at T > 100°C of Au/NiO-D compared to Au/NiO-R and Au/NiO-S.

DISCUSSION

Different morphologies of NiO, nanorods (Au/NiO-R), nanodiscs (Au/NiO-D), and nanosheets (Au/NiO-S) were synthesized by hydrothermal and wet chemical synthesis and employed as supports for the preparation of Au/NiO catalysts. The different NiO architectures were decorated with Au NPs of 2 nm (nanorods and nanosheets), and 3.2 nm average size (nanodiscs). TEM/STEM investigations suggest that dominantly the Au(111) facet of the deposited Au particles was exposed on the different NiO architectures. These catalysts were evaluated for CO oxidation reaction in the temperature range of 30°C–220°C. While Au/NiO-D showed a normal temperature dependence of the activity (Arrhenius-type behavior), Au/NiO-R and Au/NiO-S exhibited an anomalous activity behavior, characterized by a U-shaped activity curve. XPS investigations revealed distinct variations of surface oxygen species, as reflected by the surface O_{ads}/O_{latt} ratio, depending on the NiO architecture. The surface O_{ads}/O_{latt}ratio decreased in the order of Au/NiO-R > Au/NiO-D > Au/NiO-S in line with the CO oxidation activity measured at 30°C. The most active catalyst Au/NiO-R in this study had the highest O_{ads}/O_{latt} ratio, which is the highest amount of facile and reactive oxygen species. Its stable rate for CO oxidation of 1.78 $mol_{CO}\ g_{Au}^{-1}\ h^{-1}$ is comparable to the most active Au/NiO- and other Au-based supported catalysts reported in the literature. DRIFTS measurement indicated that $Au^{\delta+}$ species are crucial CO adsorption sites promoting CO oxidation over all Au/NiO catalysts. Finally, the catalytic CO oxidation over Au/NiO composites should obey Mars-van Krevelen mechanism at reaction temperature of <200°C and Eley-Rideal mechanism at high temperature of >240°C, respectively.

Limitations of the study

Our study offers insights into the morphologic effect of NiO supports on tailoring the catalytic behavior in the CO oxidation. It is observed that the Au/NiO-nanosheet with dominated NiO{110} facet exhibited a normal Arrhenius-type behavior, and the Au/NiO-nanorod (dominated NiO{200} facet) and Au/NiO-nanodisc (dominated NiO{220} facet) displayed an atypical U-shaped behavior (activity vs. temperature). The experimental results combined with theoretical calculations corroborated that these different catalytic behaviors should be mainly attributed to the accumulation of carbonate/bicarbonate species on active sites of NiO supports. Au/NiO-nanorod showed a stable CO-conversion rate of 1.78 $mol_{CO}\ g_{Au}^{-1}\ h^{-1}$ at 30°C that is comparable with the reported supported Au-based systems so far. And the catalytic CO oxidation over Au/NiO should obey Mars-van Krevelen (<200°C) and Eley-Rideal mechanism (>240°C). These results might not extrapolate universally to other NiO with different morphology and facets, and the mechanism is not well revealed by *in-situ*/operando methods. Therefore, further studies on metal oxides with different morphology and facets should be necessitous to extend these findings.

STAR★METHODS

Detailed methods are provided in the online version of this paper and include the following:

- KEY RESOURCES TABLE
- RESOURCE AVAILABILITY
  - Lead contact
  - Materials availability
  - Data and code availability
- METHOD DETAILS
  - Synthesis of NiO oxides with different morphologies
  - Preparation of Au/NiO catalysts
  - Catalytic investigations
  - Characterization
  - Computational methods

SUPPLEMENTAL INFORMATION

Supplemental information can be found online at https://doi.org/10.1016/j.isci.2024.110255.

ACKNOWLEDGMENTS

We acknowledge the financial support from Natural Science Foundation of China (no. 22172167 and 22272112).

AUTHOR CONTRIBUTIONS

Conceptualization, G.L. and Z.Z.; methodology, S.B., Y.W., Y.Z. X.G., Z.L., and B.W.; formal analysis, S.B., Y.W. and Y.Z.; investigation, S.B. and Y.W.; writing – original draft, S.B. and Y.W.; writing – review and editing, G.L., B.W., and Z.Z.; funding acquisition, G.L. and Z.Z.; visualization, S.B. and B.W.; supervision, G.L. and Z.Z.; project administration, G.L. and Z.Z.

DECLARATION OF INTERESTS

The authors declare no competing interests.

Received: April 10, 2024
Revised: May 10, 2024
Accepted: June 10, 2024
Published: June 12, 2024

REFERENCES

1. Xu, Z., Zhang, Y., Li, X., Qin, L., Meng, Q., Zhang, G., Fan, Z., Xue, Z., Guo, X., Liu, Q., et al. (2019). Template-free synthesis of stable cobalt manganese spinel hollow nanostructured catalysts for highly water-resistant CO oxidation. iScience *21*, 19–30. https://doi.org/10.1016/j.isci.2019.10.013.
2. Hu, S., Huang, M., Li, J., He, J., Xu, K., Rao, X., Cai, D., and Zhan, G. (2023). Tailoring the electronic states of Pt by atomic layer deposition of Al_2O_3 for enhanced CO oxidation performance: Experimental and theoretical investigations. Appl. Catal., B *333*, 122804. https://doi.org/10.1016/j.apcatb.2023.122804.
3. Song, Y., Hu, S., Cai, D., Xiao, J., Zhou, S.F., and Zhan, G. (2022). Cobalt phthalocyanine supported on mesoporous CeO_2 as an active molecular catalyst for CO oxidation. ACS Appl. Mater. Interfaces *14*, 9151–9160. https://doi.org/10.1021/acsami.1c23582.
4. Haruta, M., Yamada, N., Kobayashi, T., and Iijima, S. (1989). Gold catalysts prepared by coprecipitation for low-temperature oxidation of hydrogen and of carbon monoxide. J. Catal. *115*, 301–309. https://doi.org/10.1016/0021-9517(89)90034-1.
5. Shi, Q., Qin, Z., Sharma, S., and Li, G. (2021). Recent Progress in Heterogeneous Catalysis by Atomically and Structurally Precise Metal Nanoclusters. Chem. Rec. *21*, 879–892. https://doi.org/10.1002/tcr.202100001.
6. Huang, Z., Hu, S., Xu, Y., He, J., Cai, D., Sun, K., Jiang, J., and Zhan, G. (2023). Water promoting effect in CO oxidation over N-doped Co3O4/Pt nanocatalysts by tailoring metal-support interfaces. Chem Catal. *3*, 100692. https://doi.org/10.1016/j.checat.2023.100692.
7. Meyer, R., Lemire, C., Shaikhutdinov, S.K., and Freund, H.-J. (2004). Surface chemistry of catalysis by gold. Gold Bull. *37*, 72–124. https://doi.org/10.1007/bf03215519.
8. Haruta, M. (2011). Role of perimeter interfaces in catalysis by gold nanoparticles. Faraday Discuss *152*, 11–32. https://doi.org/10.1039/c1fd00107h.
9. Stephen, A., Hashmi, K., and Hutchings, G.J. (2006). Gold Catalysis. Angew. Chem. *45*, 7896–7936. https://doi.org/10.1038/s41598-018-22976-5.
10. Qin, Z., Hu, S., Han, W., Li, Z., Xu, W.W., Zhang, J., and Li, G. (2022). Tailoring optical and photocatalytic properties by single-Ag-atom exchange in Au13Ag12(PPh3)10Cl8 nanoclusters. Nano Res. *15*, 2971–2976. https://doi.org/10.1007/s12274-021-3928-4.
11. Shi, Q., Zhang, X., Li, Z., Raza, A., and Li, G. (2023). Plasmonic Au nanoparticle of a Au/TiO_2–C_3N_4 heterojunction boosts up photooxidation of benzyl alcohol using LED light. ACS Appl. Mater. Interfaces *15*, 30161–30169. https://doi.org/10.1021/acsami.3c03451.
12. Fan, L., Dai, J., Huang, Z., Xiao, J., Li, Q., Huang, J., Zhou, S.F., and Zhan, G. (2020). Biomimetic Au/CeO_2 catalysts decorated with hemin or ferrous phthalocyanine for improved CO oxidation via local synergistic effects. iScience *23*, 101852. https://doi.org/10.1016/j.isci.2020.101852.
13. Haruta, M. (1997). Size- and support-dependency in the catalysis of gold. Catal. Today *36*, 153–166. https://doi.org/10.1016/s0920-5861(96)00208-8.
14. Shao, B., Zhao, W., Miao, S., Huang, J., Wang, L., Li, G., and Shen, W. (2019). Facet-dependent anchoring of gold nanoparticles on TiO_2 for CO oxidation. Chin. J. Catal. *40*, 1534–1539. https://doi.org/10.1016/s1872-2067(19)63388-7.
15. Ide, M.S., and Davis, R.J. (2014). The important role of hydroxyl on oxidation catalysis by gold nanoparticles. Acc. Chem. Res. *47*, 825–833. https://doi.org/10.1021/ar4001907.
16. Liu, W., Yang, X., and Xie, L. (2007). Size-controlled gold nanocolloids on polymer microsphere-stabilizer via interaction between functional groups and gold nanocolloids. J. Colloid Interface Sci. *313*, 494–502. https://doi.org/10.1016/j.jcis.2007.04.055.
17. Huang, X., Liao, X., and Shi, B. (2011). Synthesis of highly active and reusable supported gold nanoparticles and their catalytic applications to 4-nitrophenol reduction. Green Chem. *13*, 2801. https://doi.org/10.1039/c1gc15873b.
18. Rahman, Z.u., Ma, Y., Hu, J., Xu, Y., Wang, W., and Chen, X. (2014). Preparation and characterization of magnetic gold shells using different sizes of gold nanoseeds and their corresponding effects on catalysis. RSC Adv. *4*, 5012. https://doi.org/10.1039/c3ra44434a.
19. Sinha, A.K., Seelan, S., Tsubota, S., and Haruta, M. (2004). Catalysis by gold nanoparticles, epoxidation of propene. Top. Catal. *29*, 95–102. https://doi.org/10.1023/B:TOCA.0000029791.69935.53.
20. Lee, S., Molina, L.M., López, M.J., Alonso, J.A., Hammer, B., Lee, B., Seifert, S., Winans, R.E., Elam, J.W., Pellin, M.J., and Vajda, S. (2009). Selective propene epoxidation on immobilized Au_{6-10} clusters, the effect of hydrogen and water on activity and selectivity. Angew. Chem. Int. Ed. *48*, 1467–1471. https://doi.org/10.1002/anie.200804154.
21. Lin, J., Abroshan, H., Liu, C., Zhu, M., Li, G., and Haruta, M. (2015). Sonogashira cross-coupling on the Au(111) and Au(100) facets of gold nanorod catalysts: Experimental and computational investigation. J. Catal. *330*, 354–361. https://doi.org/10.1016/j.jcat.2015.07.020.
22. Taketoshi, A., and Haruta, M. (2014). Size- and structure-specificity in catalysis by gold clusters. Chem. Lett. *43*, 380–387. https://doi.org/10.1246/cl.131232.
23. Sankar, M., He, Q., Engel, R.V., Sainna, M.A., Logsdail, A.J., Roldan, A., Willock, D.J., Agarwal, N., Kiely, C.J., and Hutchings, G.J. (2020). Role of the support in gold-containing nanoparticles as heterogeneous catalysts. Chem. Rev. *120*, 3890–3938. https://doi.org/10.1021/acs.chemrev.9b00662.
24. Bond, G.C., and Thompson, D.T. (2000). Gold-catalysed oxidation of carbon monoxide. Gold Bull. *33*, 41–50. https://doi.org/10.1007/BF03216579.
25. Haruta, M., and Daté, M. (2001). Advances in the catalysis of Au nanoparticles. Appl. Catal. A *222*, 427–437. https://doi.org/10.1016/S0926-860X(01)00847-X.
26. Kung, M.C., Davis, R.J., and Kung, H.H. (2007). Understanding Au-catalyzed low-temperature CO oxidation. J. Phys. Chem. C *111*, 11767–11775. https://doi.org/10.1021/jp072102i.
27. Schubert, M.M., Hackenberg, S., van Veen, A.C., Muhler, M., Plzak, V., and Behm, R. (2001). CO Oxidation over Supported Gold Catalysts—"Inert" and "Active" Support Materials and Their Role for the Oxygen Supply during Reaction. J. Catal. *197*, 113–122. https://doi.org/10.1006/jcat.2000.3069.
28. Shi, Q., Zhang, Y., Li, Z., Han, Z., Xu, L., Baiker, A., and Li, G. (2023). Morphology effects in $MnCeO_x$ solid solution-catalyzed NO reduction with CO: Active sites, water tolerance, and reaction pathway. Nano Res. *16*, 6951–6959. https://doi.org/10.1007/s12274-023-5407-6.
29. Zhang, Y., Li, Z., Cao, C., Hammedi, T., Waheed, A., Sami, B., Zhao, Z., and Li, G. (2024). Support effects on nickel hydroxide and oxide nanorods supported Au nanoparticles for CO oxidation. Catal. Lett.

154, 1026–1036. https://doi.org/10.1007/s10562-023-04368-1.

30. Xu, X., Fu, Q., Guo, X., and Bao, X. (2013). A highly active "NiO-on-Au" surface architecture for CO oxidation. ACS Catal. *3*, 1810–1818. https://doi.org/10.1021/cs400197t.
31. Zhou, S., Yin, H., Schwartz, V., Wu, Z., Mullins, D., Eichhorn, B., Overbury, S.H., and Dai, S. (2008). In situ phase separation of NiAu alloy nanoparticles for preparing highly active Au/NiO CO oxidation catalysts. ChemPhysChem *9*, 2475–2479. https://doi.org/10.1002/cphc.200800587.
32. Fang, Q., Qin, Z., Shi, Y., Liu, F., Barkaoui, S., Abroshan, H., and Li, G. (2019). Au/NiO composite, a catalyst for one-pot cascade conversion of furfural. ACS Appl. Energy Mater. *2*, 2654–2661. https://doi.org/10.1021/acsaem.9b00001.
33. Mochizuki, C., Inomata, Y., Yasumura, S., Lin, M., Taketoshi, A., Honma, T., Sakaguchi, N., Haruta, M., Shimizu, K.i., Ishida, T., and Murayama, T. (2022). Defective NiO as a stabilizer for Au single-atom catalysts. ACS Catal. *12*, 6149–6158. https://doi.org/10.1021/acscatal.2c00108.
34. Shi, Y., Tian, S., Shi, Q., Zhang, Y., Waheed, A., Cao, Y., and Li, G. (2019). Cascade aldol condensation of an aldehyde *via* the aerobic oxidation of ethanol over an Au/NiO composite. Nanoscale Adv. *1*, 3654–3659. https://doi.org/10.1039/C9NA00412B.
35. Bose, P., Ghosh, S., Basak, S., and Naskar, M.K. (2016). A facile synthesis of mesoporous NiO nanosheets and their application in CO oxidation. J. Asian Ceram. Soc. *4*, 1–5. https://doi.org/10.1016/j.jascer.2016.01.006.
36. Wang, W., Liu, Y., Xu, C., Zheng, C., and Wang, G. (2002). Synthesis of NiO nanorods by a novel simple precursor thermal decomposition approach. Chem. Phys. Lett. *362*, 119–122. https://doi.org/10.1016/s0009-2614(02)00996-x.
37. Zhang, Y., Li, Z., Zhang, J., Xu, L., Han, Z.K., Baiker, A., and Li, G. (2023). Nanostructured Ni-MoCx: An efficient non-noble metal catalyst for the chemoselective hydrogenation of nitroaromatics. Nano Res. *16*, 8919–8928. https://doi.org/10.1007/s12274-023-5598-x.
38. Zhao, B., Ke, X.K., Bao, J.H., Wang, C.L., Dong, L., Chen, Y.W., and Chen, H.L. (2009). Synthesis of flower-like NiO and effects of morphology on its catalytic properties. J. Phys. Chem. C *113*, 14440–14447. https://doi.org/10.1021/jp904186k.
39. Wei, X., Barkaoui, S., Chen, J., Cao, G., Wu, Z., Wang, F., and Li, G. (2021). Investigation of Au/Co_3O_4 nanocomposites in glycol oxidation by tailoring Co_3O_4 morphology. Nanoscale Adv. *3*, 1741–1746. https://doi.org/10.1039/d1na00053e.
40. Odio, O.F., Lartundo-Rojas, L., Santiago-Jacinto, P., Martínez, R., and Reguera, E. (2014). Sorption of gold by naked and thiol-capped magnetite nanoparticles, An XPS approach. J. Phys. Chem. C *118*, 2776–2791. https://doi.org/10.1021/jp409653t.
41. Wang, Y., Widmann, D., Lehnert, F., Gu, D., Schüth, F., and Behm, R.J. (2017). Avoiding self-poisoning, a key feature for the high activity of Au/$Mg(OH)_2$ catalysts in continuous low-temperature CO oxidation. Angew. Chem. Int. Ed. *56*, 9597–9602. https://doi.org/10.1002/anie.201702178.
42. Szabó, E.G., Hegedűs, M., Lónyi, F., Szegedi, Á., Datye, A.K., and Margitfalvi, J.L. (2009). Preparation, characterization and activity of Au/Al_2O_3 catalysts modified by MgO. Catal. Commun. *10*, 889–893. https://doi.org/10.1016/j.catcom.2008.12.019.
43. Jia, C.-J., Liu, Y., Bongard, H., and Schüth, F. (2010). Very low temperature CO oxidation over colloidally deposited gold nanoparticles on $Mg(OH)_2$ and MgO. J. Am. Chem. Soc. *132*, 1520–1522. https://doi.org/10.1021/ja909351e.
44. Jia, C.-J., Schwickardi, M., Weidenthaler, C., Schmidt, W., Korhonen, S., Weckhuysen, B.M., and Schüth, F. (2011). Co_3O_4–SiO_2 nanocomposite: a very active catalyst for CO oxidation with unusual catalytic behavior. J. Am. Chem. Soc. *133*, 11279–11288. https://doi.org/10.1021/ja2028926.
45. Liu, S., Xu, W., Liu, W., Li, L., and Wang, J. (2021). Sintering-resistant Au/iron oxide-hydroxyapatite nanocatalysts achieved by tuning strong metal-support interactions. Catal. Today *382*, 13. https://doi.org/10.1016/j.cattod.2021.01.012.
46. Zhang, T., Xu, J., Sun, Y., Fang, S., Wu, Z., Gao, E., Zhu, J., Wang, W., Dai, L., Liu, W., et al. (2023). Exploring the key components of Au catalyst during CO oxidation using TG-MS and operando DRIFTS-MS. Mol. Catal. *547*, 113361. https://doi.org/10.1016/j.mcat.2023.113361.
47. Budroni, G., and Corma, A. (2006). Gold–organic–inorganic high-surface-area materials as precursors of highly active catalysts. Angew. Chem. Int. Ed. *45*, 3328–3331. https://doi.org/10.1002/anie.200600552.
48. Okumura, M., Nakamura, S., Tsubota, S., Nakamura, T., Azuma, M., and Haruta, M. (1998). Chemical vapor deposition of gold on Al_2O_3, SiO_2, and TiO_2 for the oxidation of CO and of H_2. Catal. Lett. *51*, 53–58. https://doi.org/10.1246/cl.1998.315.
49. Bamwenda, G.R., Tsubota, S., Nakamura, T., and Haruta, M. (1997). The influence of the preparation methods on the catalytic activity of platinum and gold supported on TiO_2 for CO oxidation. Catal. Lett. *44*, 83–87. https://doi.org/10.1023/A:1018925008633.
50. Ito, S., Wang, X., Waheed, A., Li, G., Maeda, N., Meier, D.M., Naito, S., and Baiker, A. (2021). Support effects in iridium-catalyzed aerobic oxidation of benzyl alcohol studied by modulation-excitation attenuated total reflection IR spectroscopy. J. Catal. *393*, 42–50. https://doi.org/10.1016/j.jcat.2020.11.010.
51. Du, X., Huang, Y., Pan, X., Han, B., Su, Y., Jiang, Q., Li, M., Tang, H., Li, G., and Qiao, B. (2020). Size-dependent strong metal-support interaction in TiO_2 supported Au nanocatalysts. Nat. Commun. *11*, 5811. https://doi.org/10.1038/s41467-020-19484-4.
52. Chakarova, K., Mihaylov, M., Ivanova, S., Centeno, M.A., and Hadjiivanov, K. (2011). Well-defined negatively charged gold carbonyls on Au/SiO_2. J. Phys. Chem. C *115*, 21273–21282. https://doi.org/10.1021/jp2070562.
53. Hassan, J.Z., Zaheer, A., Raza, A., and Li, G. (2023). Au-Based Heterostructure Composites for Photo and Electro Catalytic Energy Conversions. Sust. Mater. Technol. *36*, e00609. https://doi.org/10.1016/j.susmat.2023.e00609.
54. Mihaylov, M., Knözinger, H., Hadjiivanov, K., and Gates, B.C. (2007). Characterization of the oxidation states of supported gold species by IR spectroscopy of adsorbed CO. Chem. Ing. Tech. *79*, 795–806. https://doi.org/10.1002/cite.200700029.
55. Chen, Y., Li, Y., Chen, W., Xu, W.W., Han, Z.k., Waheed, A., Ye, Z., Li, G., and Baiker, A. (2022). Continuous dimethyl carbonate synthesis from CO_2 and methanol over $Bi_xCe_{1-x}O_\delta$ monoliths: Effect of bismuth doping on population of oxygen vacancies, activity, and reaction pathway. Nano Res. *15*, 1366–1374. https://doi.org/10.1007/s12274-021-3669-4.
56. Kresse, G., and Furthmüller, J. (1996). Efficiency of ab-initio total energy calculations for metals and semiconductors using a plane-wave basis set. Comput. Mater. Sci. *6*, 15–50. https://doi.org/10.1016/0927-0256(96)00008-0.
57. Kresse, G., and Furthmüller, J. (1996). Efficient iterative schemes for ab initio total-energy calculations using a plane-wave basis set. Phys. Rev. B *54*, 11169–11186. https://doi.org/10.1103/physrevb.54.11169.
58. Perdew, J.P., Burke, K., and Ernzerhof, M. (1996). Generalized gradient approximation made simple. Phys. Rev. Lett. *77*, 3865–3868. https://doi.org/10.1103/physrevlett.77.3865.
59. Monkhorst, H.J., and Pack, J.D. (1976). Special points for Brillouin-zone integrations. Phys. Rev. B *13*, 5188–5192. https://doi.org/10.1103/PhysRevB.13.5188.

STAR★METHODS

KEY RESOURCES TABLE

REAGENT or RESOURCE	SOURCE	IDENTIFIER
Chemicals		
$NiSO_4 \cdot 7H_2O$	Adamas	10636BA
$NaBH_4$	Adamas	G29269C
NaOH	Adamas	G19852D
$Ni(CH_3COO)_2 \cdot 4H_2O$	Adamas	69069A
Na_2CO_3	Adamas	24073D
HAuCl4	Adamas	44406B
Software and algorithms		
Gaussian09	Frish et al.[1]	https://gaussian.com
XPSPEAK41 software	xpspeak	https://xpspeak.software.informer.com

RESOURCE AVAILABILITY

Lead contact

Further information and requests for resources should be directed to and will be fulfilled by the lead contact, Gao Li (gaoli@dicp.ac.cn).

Materials availability

This study did not generate any new materials.

Data and code availability

- All the information about the data reported here is included in this paper.
- This paper does not report original code.
- Any additional information required to reanalyze the data reported in this paper is available from the lead contact upon request.

METHOD DETAILS

Synthesis of NiO oxides with different morphologies

The synthesis routes of the Au-NiO nanocatalysts supported on the morphologically different NiO is illustrated in scheme S1. NiO oxide nanorods (denoted as NiO-R) were prepared via a hydrothermal method. In brief, 19.6 mmol of nickel sulfate hexahydrate ($NiSO_4 \cdot 6H_2O$), in 40 mL water, was led to react with 6.6 mmol of sodium hydroxide (NaOH, in 40 mL water), pH ~7.3 in a Teflon-lined autoclave. After vigorously stirring for 30 min, the temperature was ramped up to 120°C for 24 h. The precipitates were washed several times with water and methanol before drying at 80°C, and then calcined at 400°C for 2 h yielding NiO-R.

NiO nanodiscs (denoted as NiO-D) were prepared using a similar hydrothermal method. 2.45 mmol $NiSO_4 \cdot 6H_2O$ (40 mL water) was let to react with 3.3 mmol of NaOH (in 40 mL water) at 40°C and kept 3 h under stirring. The reaction temperature and time in the autoclave were the same as those used for the preparation of the nanorods. However, the calcination was carried out at 300°C for 3 h yielding NiO-D. The nanosheet-like NiO (NiO-S) was synthesized via a wet chemical synthesis method by dissolving 0.05 mol of nickel acetate tetrahydrate ($Ni(CH_3COO)_2 \cdot 4H_2O$) in ethylene glycol in a 1L round bottom flask at 120°C for 0.5 h under magnetic stirring. Then 0.5 L of aqueous sodium carbonate (Na_2CO_3, 0.2 M) solution was added dropwise (2 mL min^{-1}) to the above mixture. After the addition of the aqueous solution of Na_2CO_3, the mixture was kept at 120°C for 1 h. Then, it was cooled to room temperature and the precipitates were washed several times with distilled H_2O and ethanol before drying at 80°C overnight. The dried product was calcined at 300°C for 3 h yielding NiO-S.

Preparation of Au/NiO catalysts

The deposition of gold nanoparticles on the differently shaped NiO samples was achieved by impregnation with a nominal Au loading of ca. 1 wt %. 1 g of NiO support was added to the colloidal gold solution, which was prepared using PVA (polyvinyl alcohol). After stirring for 3 h, Au/NiO catalysts were washed with water and ethanol and then calcined at 300°C in air to remove the organic surfactant as evidenced by temperature-programmed oxidation (O_2-TPO) analysis. ICP-MS confirmed that the Au loadings of the Au/NiO-R, Au/NiO-S, and Au/NiO-D were ~0.90 wt %.

Catalytic investigations

CO oxidation was conducted in a continuous flow tubular fixed-bed glass reactor with an inner diameter of 1 cm. Before the tests, samples were pretreated at 300°C using a 20%O_2/He mixed gas and then cooled down to ca. 30°C. The feed gas (1%CO/20%O_2/He) of 50 mL min^{-1} was passed over the catalyst corresponding to a gas hourly space velocity (GHSV) of ~60,000 mL g_{cat}^{-1} h^{-1}. The catalytic behavior was investigated by raising the temperature from 30°C to 220°C. At each indicated reaction temperature, data were acquired after 1 h and confirmed by repetitive runs. In addition, long-term experiments were carried out to test the stability of the catalysts. The amounts of CO and CO_2 at the outlet streams of the reactor were analyzed by an online gas chromatograph. The conversion of CO (X_{CO}) was calculated based on the measured CO consumption and CO_2 formation and calculated according to:

$$X_{CO} = \frac{C_{CO,in} - C_{CO,out}}{C_{CO,in}} \times 100\%$$

where, $C_{CO,in}$ and $C_{CO,out}$ are the concentrations of the gases at the reactor inlet and outlet.

Characterization

The powder X-ray diffraction patterns were recorded using an X-ray powder diffractometer (SmartLab) with Cu Kα radiation at 40 kV and 30 mA in the 10° to 70° at a scan rate of 10° min^{-1}. The specific surface area of the supports was determined on a Micromeritics ASAP 2020 surface analyzer (Quantachrome) using nitrogen adsorption at 77 K and the BET method. The samples were pretreated at 400°C in a vacuum overnight before the isotherm measurements. The pore size distributions were calculated from the desorption isotherms employing the Barret-Joyner-Halenda method. Scanning transmission electron microscopy (STEM) images were recorded on an F200 microscope operated at 300 kV. The specimen was prepared by ultrasonically dispersing the sample into ethanol, and depositing droplets of the suspension onto a carbon-enhanced copper grid, followed by drying them in air. Transmission electron microscopy (TEM) images were recorded on a FEI Tecnai G2 Spirit microscope operated at 120 kV. X-ray photoelectron spectra (XPS) were measured on an ESCALAB MK-II spectrometer using an aluminum anode for Kα (hv1484.6 eV) radiation. The equipment base pressure was 1.7×10^{-10} mbar, and all samples were characterized at room temperature. Detailed spectra were recorded for the region of Ni 2p, O1s, and Au 4f photoelectrons using a 0.1 eV step. Analysis was performed by the XPSPEAK41 software, and charging effects were corrected by adjusting the binding energy (B.E.) of C1s to 284.6 eV. The spectra were deconvoluted using the XPSPEAK program by curve-fitting with a mixed Gaussian-Lorentzian function. Fourier transform infrared (FT-IR) measurements were recorded on a Bruker VERTEX 70 instrument equipped with Bruker HYPERION 3000. The sample was firstly pretreated at 300°C for 1 h under O_2/He with a flow rate of 25 mL min^{-1} to eliminate water traces. After the sample was cooled to room temperature in a helium flow (25 mL min^{-1}), the background spectra were recorded and used as references. Then the flowing gas was switched to 1 vol % CO/He and the spectra were collected. Inductively coupled plasma-mass spectrometry (ICP-MS) was conducted on PerkinElmer ICP-MS NexION 300D. The samples were dissolved in an aqua regia solution (HCl: HNO_3 = 3:1 v/v) at 80°C for 2 h, and then the solution was diluted with Nanopure water (resistance 18.2 MX cm, purified with a Barnstead NANO pure Di-water TM system) in a volumetric flask before the test. CO_2-temperature programmed desorption (CO_2-TPD) was carried out on a Micromeritics Autochem II chemosorption analyzer. Before measurements, 100 mg of Au/NiO (40–60 mesh) were packed into the quartz reactor and pretreated for 2 h in a He flow of 20 mL min^{-1} at 400°C. Afterward, the reactor was cooled down to room temperature and the sample was saturated with 10 vol % CO_2 (balanced by He) at room temperature. The desorption profiles were recorded by ramping the reactor temperature up to ~500°C at a heating rate of 10°C min^{-1}. The evolving CO_2 species (*m/z* 44) were monitored online by GC-MS.

Computational methods

The calculations were performed using the Vienna ab initio simulation package code (VASP).[56] The wave function was expanded by the plane wave, with a kinetic cut-off of 520 eV. The generalized gradient approximation with the spin-polarized Perdew–Burke–Ernzerhof (PBE) functional was used.[57,58] The convergence tolerance for residual force and energy on each atom during structure optimization was set to 0.02 eV/Å and 10^{-4} eV, respectively. The periodically repeated slabs on the surface were decoupled by 15 Å vacuum gaps. A Monkhorst–Pack grid of (2 × 2 × 1) k-points was used in the calculations. Besides, the bottom half atoms were fixed to bulk while the others are relaxed.[59]